Acta Astronautica 109 (2015) 132–143

Contents lists available at ScienceDirect

Acta Astronautica

journal homepage: www.elsevier.com/locate/actaastro

Review

Development of DBD plasma actuators: The double encapsulated electrode

Rasool Erfani [a,*], Hossein Zare-Behtash [b], Craig Hale [b], Konstantinos Kontis [b]

[a] Manchester Metropolitan University, School of Engineering, Manchester, M1 5GD, UK
[b] University of Glasgow, School of Engineering, Glasgow, G12 8QQ, UK

ARTICLE INFO

Article history:
Received 5 September 2014
Received in revised form
15 November 2014
Accepted 30 December 2014
Available online 19 January 2015

Keywords:
Plasma actuator
Dielectric barrier discharge

ABSTRACT

Plasma actuators are electrical devices that generate a wall bounded jet without the use of any moving parts. For aerodynamic applications they can be used as flow control devices to delay separation and augment lift on a wing. The standard plasma actuator consists of a single encapsulated (ground) electrode. The aim of this project is to investigate the effect of varying the number and distribution of encapsulated electrodes in the dielectric layer. Utilising a transformer cascade, a variety of input voltages are studied for their effect. In the quiescent environment of a Faraday cage the velocity flow field is recorded using particle image velocimetry. Through understanding of the mechanisms involved in producing the wall jet and the importance of the encapsulated electrode a novel actuator design is proposed. The actuator design distributes the encapsulated electrode throughout the dielectric layer. The experiments have shown that actuators with a shallow initial encapsulated electrode induce velocities greater than the baseline case at the same voltage. Actuators with a deep initial encapsulated electrode are able to induce the highest velocities as they can operate at higher voltages without breakdown of the dielectric.

Contents

* Corresponding author. Tel.: +44 161 247 6219.
E-mail address: r.erfani@mmu.ac.uk (R. Erfani).

http://dx.doi.org/10.1016/j.actaastro.2014.12.016
0094-5765/

1. Introduction

The manipulation of the flow over aircraft wings has been the subject of intense research as the appropriate solution can yield a great number of benefits. Such techniques focus on the manipulation of the boundary layer, a thin layer located close to the wall of an object travelling through a fluid. Successful control of this region allows for increased lift performance and drag reduction. These in turn allow for lower take-off and landing speeds, shorter runways, increased endurance, improved manoeuvrability and lower fuel consumption to name a few. In today's economic and environmental climate, coupled with the human desire to travel, there is a great requirement for the benefits that can be provided. The benefit of such flow control techniques is not the costs but the ability to directly compete with the rugged and thoroughly proven technology of the conventional aircraft flow control devices such as flaps and slats.

Recently a new flow control technique has been investigated that has the potential to achieve this, namely, the single dielectric barrier discharge (SDBD) plasma actuator. These have been extensively studied over the last decade [1–3]. A typically SDBD system consists of two electrodes offset in the chordwise direction and separated by a dielectric layer, typically Kapton, glass, quartz or ceramics. The encapsulated electrode is connected to the earth and the exposed electrode is attached to a high voltage supply. Typical required voltages are in the kV range and applied with an a.c. frequency in the kHz range. When activated, a purplish glow plasma is visible, originating at the exposed electrode and spreading out across the dielectric surface that is above the encapsulated electrode as shown in Fig. 1. The plasma is ionised air consisting of ions and electrons with the bulk plasma exhibiting electrical neutrality. The remarkable aspect of this arrangement is that it has the ability to produce a steady jet that flows away from the exposed electrode across the encapsulated electrode on the scale of seconds, without the need for any moving parts. The plasma actuator is lightweight, easy to repair, flexible and able to follow the curvature of the surface it is applied to. It can be switched on or off or passive at the flick of a switch, can be activated at a wide range of modulation frequencies and has a high frequency response. The entire system is all-electric and fits in well with the current ethos of aircraft manufacturers to produce all electric aircrafts.

Many studies have been conducted to optimise the plasma actuator in an attempt to improve performance [4–6]. Variables that influence plasma distribution and intensity are voltage waveform, voltage amplitude, frequency, electrode configurations, background gas, dielectric material, dielectric thickness and dielectric temperature [7–10]. Optimisation of the plasma actuator has shown the importance of the supplied signal as well as the geometry of the electrodes [11,12]. Correct material selection, especially for the dielectric layer, can lead to large performance gains most notably from the reduction of dielectric heating [13,11]. Currently plasma actuators lack the induced momentum to directly compete with pneumatic systems, restricting them to low Reynolds number flows [14–16]. Further understanding of the plasma actuator mechanism for jet production or techniques to further enhance the momentum addition are vital to establishing the plasma actuator as a legitimate full scale flow control technique.

The motivation behind the current investigation is to optimise the actuator and increase the maximum induced velocity. This is achieved through a novel actuator design that varies the distribution of the encapsulated electrode in the dielectric layer [17–19].

2. Experimental setup

2.1. High-voltage generation system

The high voltage generation system is composed of a Voltcraft 3610 power supply that is capable of outputting a maximum of 36 V when operating in constant voltage mode or a maximum of 10 A when operating in constant current mode. The maximum power that can be produced by the power supply is 360 W. The power supply is connected to a control circuit board manufactured by Electrofluidsystems that is able to output a variety of signals. The control circuit board is connected to a PC via a National instruments BNC-2110 shielded connector block and PCI-6713 analog output card. The PC operates a LabView program where the plasma driving frequency, modulation frequency, duty cycle and signal shape can be varied. The maximum output frequency is 30 kHz and a full 0–100% duty cycle can be used.

The signal input, from the control circuit board, and the power input, from the Voltcraft 3610, are combined to produce the desired output signal. The output signal is connected to a Minipuls 6 cascade transformer designed and manufactured by Electrouidsystems. The transformer is capable of a 30 kHz output signal at voltages of up to 40 kV_{p-p}. A transformer cascade is able to output high voltages using small individual transformer components compared to a single stage transformer.

The output voltage and frequency from the transformer is measured using a LeCroy PPE-20 kV high voltage probe that is provided with a detailed calibration from the manufacturers. The output current is measured using a current probe that is built into the transformer cascade and measures the voltage drop across a resistor. The voltage and current output signals are connected to a picoscope 3206, 250 MHz oscilloscope that is in turn connected to a PC where the signals are displayed and recorded.

2.2. Plasma actuators

2.2.1. Baseline plasma actuator

The baseline actuator consists of an exposed electrode constructed from 74 μm thick tinned copper foils, 5 mm wide and 100 in length. The encapsulated electrode is

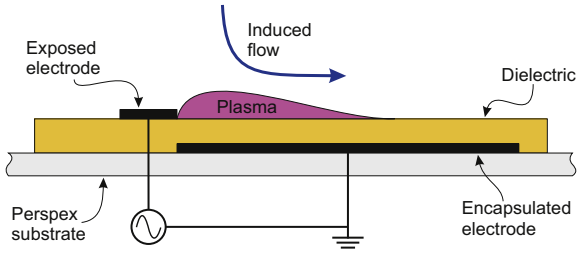

Fig. 1. Standard SDBD actuator configuration [6].

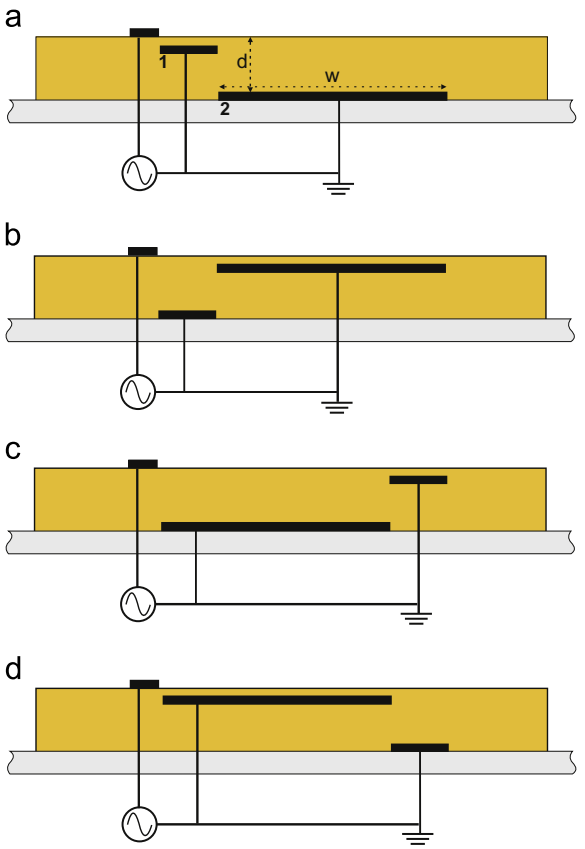

Fig. 2. Schematic of the various actuators evaluated. (a) MEE5, (b) MEE6, (c) MEE7, (d) MEE8.

Table 1
Different MEE-SDBD configurations.

Case	d_1(μm)	w_1(mm)	d_2(μm)	w_2(mm)	Exposed (w) (mm)
MEE5	180	10	540	40	5
MEE6	540	10	180	40	5
MEE7	540	40	180	10	5
MEE8	180	40	540	10	5

constructed from the same material but 50 mm wide. Kapton tape with 540 μm thickness is layered on top of the encapsulated electrode with each layer having a 60 μm thickness. The actuator is mounted on a Perspex substrate and there is no offset between the edges of successive electrodes.

2.2.2. *Multiple encapsulated electrode (MEE) plasma actuator*

The overall dimensions of the MEE plasma actuator used in this study are the same as that of the baseline configuration. The difference is that instead of having a single, uniform encapsulated electrode it has multiple encapsulated electrodes that are distributed throughout the dielectric layer. The maximum depth, overall width and polarity of the encapsulated electrode remains the same throughout all configurations. In total, eight configurations of MEE plasma actuators have been investigated. The MEE configurations consist of two encapsulated electrodes. Diagrams of the MEE actuators are shown in Fig. 2. The widths and depths in the dielectric layer as well as the offset between adjacent electrodes for all the actuator cases are presented in Table 1. The lengths are proportional to each other but the thicknesses are exaggerated so that the electrodes can be seen.

2.3. *Particle image velocimetry*

A Litron Nano L series, ND:YAG Q-switched laser is used for particle image velocimetry (PIV) illumination. The laser has a pulse energy of 200 mJ per pulse with a repetition rate of 15 Hz. The laser beams are pulsed at a wavelength of 532 nm. A laser arm is used to deliver the laser to the test section. A TSI six-jet atomiser TSI model 9307-6 was used to create seeder particles with particle diameters of approximately 1 μm [20].

A LaVision Imager ProX2M CCD camera with 1600 $\times$ 1200 pixel resolution was employed to capture the scattered light from the tracer particles. The camera records images at 14 bit digitisation. The recorded image pairs are initially divided into 32 $\times$ 32 pixel interrogation windows and then processed with a cross correlation algorithm using the DaVis 7.2 software. The interrogation windows are then refined to 16 $\times$ 16 pixel squares. A 50% overlap was employed in order to improve the spatial resolution and to prevent the appearance of spurious vectors by adaptively improving the interrogation window size. The time between laser pulses was set at 400 μs based on the window size of 280 mm $\times$ 80 mm and the expected flow velocity of up to 3 m/s. This produces a shift of 5 pixels between images which is within the range of 3–8 pixels to obtain highly accurate results. Post processing used two passes of 8 $\times$ 8 pixel interrogation zones with a 50% overlap to calculate the velocity fields. Each measurement run produced 100 velocity flow fields that were averaged to produce the time averaged plasma wall jet. This is a method that has been used extensively by Enloe et al. [7], Post and Corke [21], Santhanakrishnan and Jacob [22] to characterise the plasma wall jet and determine maximum jet velocity. For each voltage and frequency setting 3 runs were conducted and showed close correlation between the data sets.

The repeatability of the PIV experiments is determined by providing the plasma actuator with a set input voltage and driving frequency. The image acquisition was conducted at the same time interval after the start of the actuator and the same number of PIV images is taken. Each measurement run produced 100 velocity fields that were

averaged to produce a time averaged plasma wall jet. For each voltage and frequency setting 3 runs were conducted and showed close correlation between the data sets. Activation of the actuator without the presence of any filaments produces repeatability in the peak velocity of $\pm 1\%$ and for a filamentary plasma the accuracy is $\pm 10\%$.

2.4. Light intensity measurements

The plasma actuators were mounted in the top section of the Faraday cage with the cage sealed to eliminate any light contamination. A LaVision Intensified CCD camera with 1024 $\times$ 1024 pixels was orientated normal to the plasma actuator and viewed the full spanwise width. 100 images at an exposure time of 1 ms were recorded for each plasma actuator at the varying voltages. This produced an image representing 10 cycles of the plasma actuator when operating at 10 kHz. The average plasma extension for the different actuator configurations are recorded and compared. A dark image was also taken before each measurement and subtracted from the plasma images during post processing in Matlab.

3. Results and discussion

3.1. Electrical characteristics and power consumption

When one of the electrodes in the configuration is provided with sufficient voltage and frequency magnitude, low current discharges will appear in the current trace. The current discharges occur because the breakdown field strength of the gas in the discharge gap has been reached, resulting in the formation of a plasma that appears constant to the naked eye. Each individual discharge is small, termed microdischarges, and is distributed across the electrodes. The microdischarge is a small channel of charge that lasts on the order of ns, and terminates on the dielectric surface. There is a build up of charge on the dielectric surface that reduces the electric field strength across the discharge gap leading to the termination of the discharge.

Throughout the literature the current trace has been used to describe the plasma characteristics [8]. It is known that the current curve consists of a displacement component that is 90° out of phase with the applied voltage. The displacement current has been attributed to electric field lines that directly connect the charged and grounded electrodes and is present irrespective of the plasma state [7,12]. A component of the current that is highly visible is the plasma 'grass' that is the result of a number of microdischarges and only occurs when the plasma is present. The plasma is present twice during one voltage cycle representing the forward stroke (FS), negative-going, and backward stroke (BS), positive-going. The two discharges in the cycle differ between a relatively uniform discharge, consisting of microdischarges of similar amplitudes, during the BS and a patchy irregular discharge, consisting of fewer, larger discharges during the FS, see Fig. 3.

The FS ignition point, FS_i, is measured from the point where there is a change in the displacement current. This is either the appearance of the microdischarges, seen as the 'grass', or a point of inflection. In the initial instance a point of inflection is seen to occur and it immediately followed by the appearance of the microdischarge current. Applying the same principles to the BS ignition point, BS_i, a point of inflection is measured for different cases. The quench point of the FS and BS, FS_q and BS_q respectively, is measured as the point where the variation of data is of a magnitude comparable to the displacement only portions

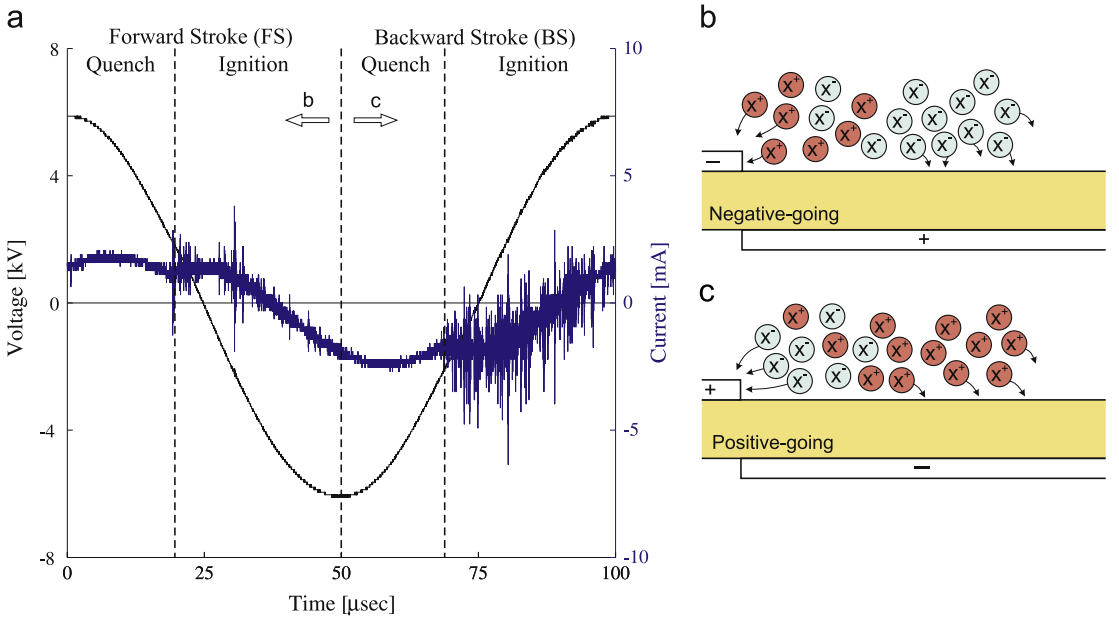

Fig. 3. Voltage and current traces of baseline configuration, 12 kV_{p-p} and 10 kHz (a), when electrons leave the exposed electrode (b), and some deposited electrons returning (c) (subfigures (b) and (c) are not to scale).

of the current cycle. Although only one voltage cycle is shown, the cycle is constant for many periods and the quenching of the BS can be taken as being at the same position in the following cycle. This allows for BS_q to also be taken and used to calculate the portion of the cycle that the BS plasma is present. Using these time points, four further parameters can be calculated, the two time gaps between the two strokes and the length of time that each stroke is present.

The FS considered the part of the stroke that contributes the most to momentum coupling since it present longer than the BS.

It was shown that there is a relaxation of a pressure builds up at the exposed electrode that is released during the quenching phase after the FS [23]. These current characteristics show that the time available for this relaxation to take place is longer than the quenching period after the BS.

At FS_i, the electrons are readily available to leave the exposed electrode and deposit themselves upon the dielectric surface, Fig. 3(b). During the BS a slightly different mechanism is involved as the electrons have to be released from the dielectric surface and returned to the exposed electrode, Fig. 3(c). A dielectric surface does not as readily give up the electrons as the electrode surface does so a slightly higher magnitude of dV/dt is required to overcome the initial resistance and ignite the plasma. The ignition point of the plasma is sensitive to dV/dt with plasma igniting once the breakdown value of the background gas has been achieved. The point in time at which this critical value will occur varies with applied voltage magnitude and occurs earlier in the cycle at higher voltages.

The current traces for the double encapsulated electrode actuators and the baseline case are presented in Fig. 4 for a voltage of 12 kV_{p-p} and frequency of 10 kHz. The two plasma stroke characteristics are evident in the figure. Dash lines represent the characteristics of the current trace of baseline case illustrated in Fig. 3.

The MEE6 and MEE7 cases have ignition and quench times that occur at the same points in the cycle as the standard actuator case. This is due to the initial electrode

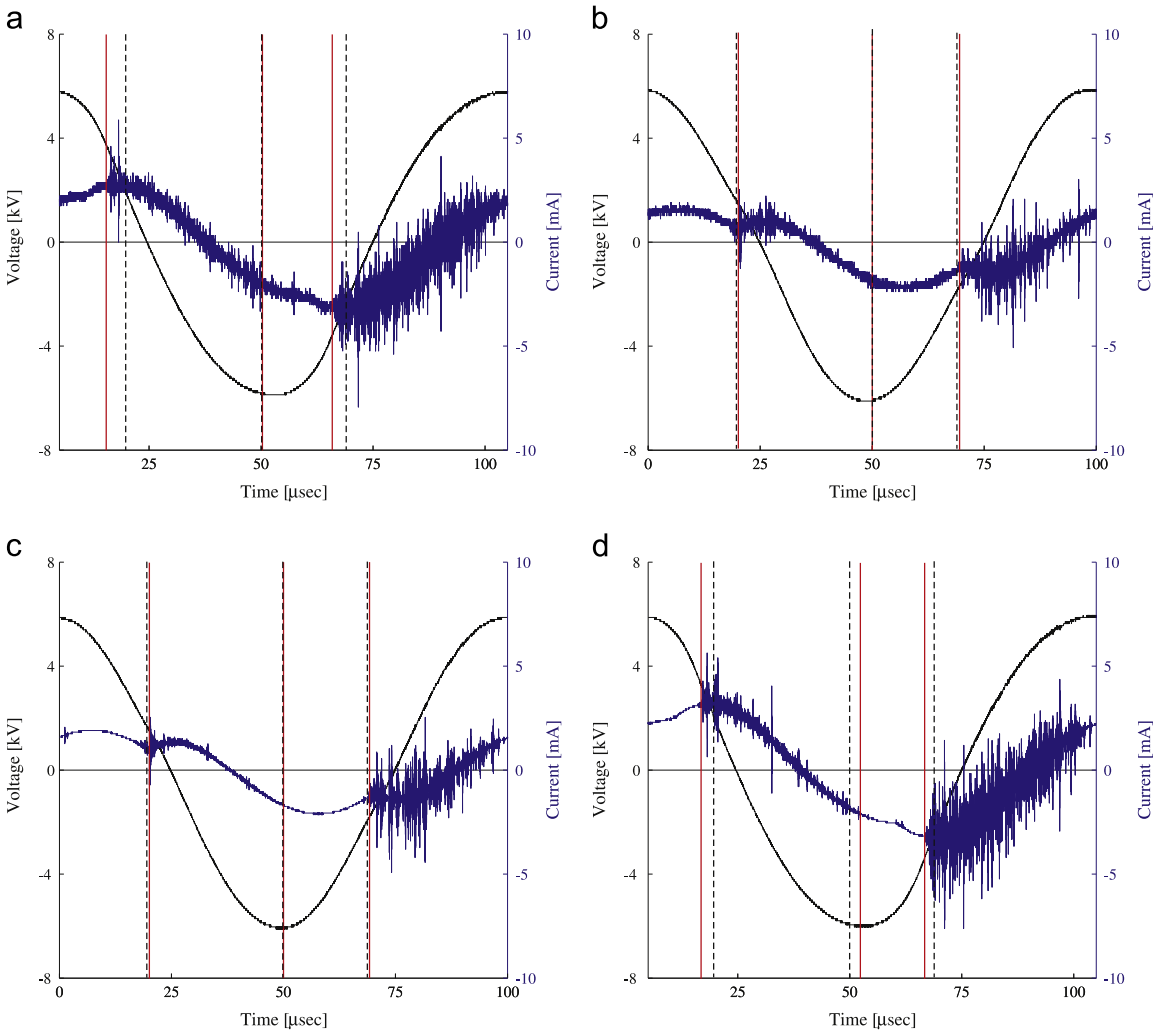

Fig. 4. Voltage and current traces for input voltage of 12 kV_{p-p} and frequency of 10 kHz; (a) MEE5, (b) MEE6, (c) MEE7 and, (d) MEE8.

being at the same depth for these cases. All of the double encapsulated electrode cases have BS that last longer than the FS.

This highlights that varying the depth of the encapsulated electrode far downstream of the exposed electrode has limited effect on the ignition and quench times of the plasma. The shallow initial electrode actuator cases show a contraction of the quench period and an expansion of the plasma present periods compared to the standard actuator case. The presence of a shallow initial electrode allows the electric field to reach the breakdown field strength earlier in the cycle for the FS and BS. The change in depth of the encapsulated electrode downstream of the initial encapsulated electrode has no effect on the ignition and quenches times of the plasma.

The deep initial electrode cases have plasma present periods that last the same length of time as the standard actuator case. Having the initial electrode closer to the surface lengthens the plasma present periods and as a result shortens the quench periods. The MEE5 and MEE8 cases have plasma present times that are almost identical to each other suggesting that changing the encapsulated depth after 10 mm from the exposed electrode has limited effect on the plasma time characteristics.

The results suggest that the depth of the initial electrode determines at what point in the cycle ignition of the FS takes place. The length of the initial electrode then determines the amount of the cycle over which the FS can take place. Shallower electrodes initiate ignition earlier because the electric field strength required for breakdown occurs earlier in the voltage cycle. Longer shallow initial electrodes then allow the voltage required to sustain the discharge for longer by delaying the FS_q. As the length of time the FS lasts has increased, so has the amount of charge that has been deposited on the dielectric surface. This results in the earlier ignition of the BS as the difference in charge between the exposed electrode and virtual electrode on the dielectric surface becomes sufficiently large earlier in the cycle to initiate plasma discharge. The plasma discharge is sensitive to the electrode depth close to the exposed electrode as a slight reduction, as in the MEE5 case, results in a reduction in the amount of time the plasma is present. A deep initial electrode results in the plasma characteristics being insensitive to changes in electrode depth further downstream of the encapsulated electrode.

The power used by each actuator at the supplied voltage is calculated using Eq. (1), where T and N represent the time period and the number of cycles, respectively and is shown in Fig. 5.

$$\text{Power} = \frac{1}{NT}\int_{NT} V(t).I(t)\,dt \tag{1}$$

The MEE5 and MEE8 cases consume more power than the baseline case while the MEE6 and MEE7 actuator cases consume less. The MEE6 case required the least power using 14.32% less than the baseline case. The change in power consumption can again be explained by the positioning of the encapsulated electrodes. The MEE5 and MEE8 cases have the initial encapsulated electrode located closer to the surface and the exposed electrode. This results in the formation of stronger plasma that requires more power to be sustained. Conversely the actuators with a lower initial electrode require less power than the baseline case.

3.2. Actuator light emission

The plasma actuators were photographed to provide a long exposure image of the plasma discharge. The expansion distances for all of the actuator cases are presented in Table 2. The plasma discharge at various voltages for the baseline actuator case is shown in Fig. 6(a). As the voltage to the actuator is increased the plasma expands further over the dielectric surface, starting at the edge of the exposed electrode. The plasma consists of bright patches at the exposed electrode edge that are the result of weaknesses in the actuator construction. If a fold exists in the exposed electrode or the edge is not flush with the dielectric surface a point of high electric stress occurs. This is the point where the plasma will ignite first and as a result looks brighter in a time exposed image. The extremity of the plasma is uniform in appearance with a slight gradient in the brightness due to the plasma at the edge being present for a shorter amount of time compared to

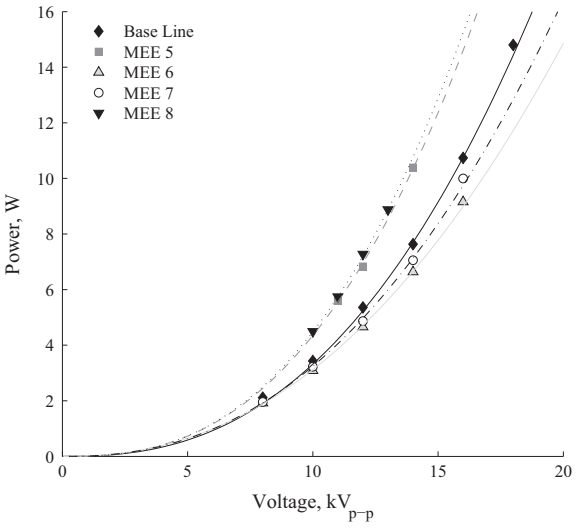

Fig. 5. Power variation with voltage for the baseline, MEE5, MEE6, MEE7 and MEE8 cases.

Table 2
Plasma expansion distances for the various voltages and actuator cases imaged.

Case	Voltage (kV_{p-p})	Expansion (mm)
Baseline	8	2.1
Baseline	10	4.1
Baseline	12	5.7
Baseline	14	6.9
Baseline	16	8.2
MEE5	12	6.3
MEE6	12	2.7
MEE7	12	2.3
MEE8	12	6.2

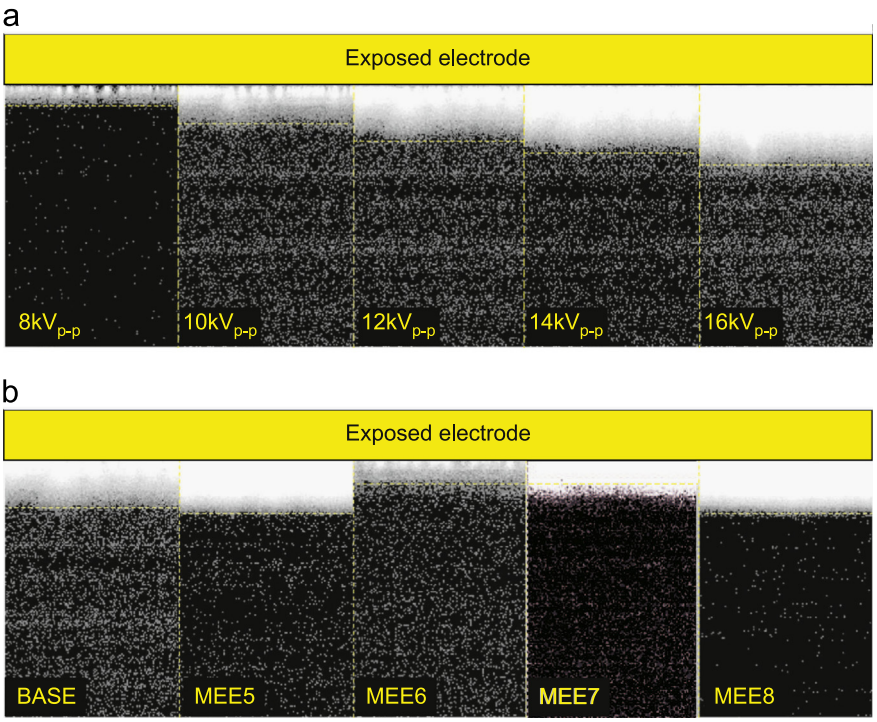

Fig. 6. Plasma expansion images: (a) baseline case for various voltages and 10 kHz, (b) double MEE at 12 kV_{p-p} and 10 kHz.

the plasma at the exposed edge [8]. At the highest voltage imaged, 16 kV_{p-p}, other structures have appeared. At the lower voltages the charge carriers are a large series of microdischarges that result in a uniform glow. At the higher voltages the plasma has degraded into coarse filaments. At 16 kV_{p-p} there are four established coarse filaments that originate from the regions of high electrical stress from actuator construction. When operating the plasma actuators in a filamentary mode the performance and lifetime of the actuator degrades. The length of plasma expansion is considerably less than the total width of the encapsulated electrode available. It is expected that the plasma extends further across the encapsulated electrode but is much weaker at these distances due to the short length of time it is present and the weaker electric field.

A shallow initial electrode produces a brighter plasma with a longer extension. This is the result of the plasma being present for longer portions of the cycle. In the MEE5 and MEE8 cases, in Fig. 6(b), coarse filaments can be seen in the plasma. The MEE6 and MEE7 cases have a plasma brightness and extension that is less than that of the baseline case. From these characteristics it can be concluded that these cases have the plasma present for less of the voltage cycle than the baseline case. As the brightness is a result of the strength and amount of time the plasma is present this result is to be expected.

3.3. Velocity profiles

The symbols in Figs. 7, 8, 9 and 11 do not represent individual PIV data points and are only used to distinguish the different actuator types.

The velocity profiles for the x-component of velocity are presented in Fig. 7 for standard SDBD actuator, baseline in figure, and MEE configurations. All MEE configurations produce an induced jet flowing from the exposed electrode across the encapsulated electrode at $x = 0$ mm in contrast to the baseline case, Fig. 7(a). For example, the MEE5 configuration is able to produce a jet of 0.5 m/s at the electrode interface. The next highest induced jet at this position is for the MEE8 configuration at 0.2 m/s. These two configurations have the first encapsulated electrode located closest to the surface. The induced jet at this x-position is likely to be a result of the down flow region being directed to a position downstream of the electrode interface. 10 mm downstream of the exposed electrode, Fig. 7(b), all actuators produce induced jets that flow across the encapsulated electrode. The MEE5 induced jet continues to increase in velocity reaching 0.6 m/s, the highest at this position. All other configurations, with the exception of MEE8, also show an increase in the induced jet velocity.

The MEE8 configuration exhibits a reduction in velocity, likely due to the lack of a down flow region to generate a V_x component and the initial jet being located the furthest from the exposed electrode. The MEE6 and MEE7 actuators produce jets with similar maximum velocity and shape, achieving 0.2 m/s. The actuators show a slight negative velocity at a height of 2–4 mm. This is due to the influence of the down flow region drawing the air down and back towards the $x=0$ mm position. At the $x=20$ mm position, Fig. 7(c), all actuators produce strong induced jets. The MEE5 jet has more than doubled its induced velocity in excess of 1.3 m/s. The baseline actuator profile at this point has a maximum away from the surface of the dielectric. At this position the actuators

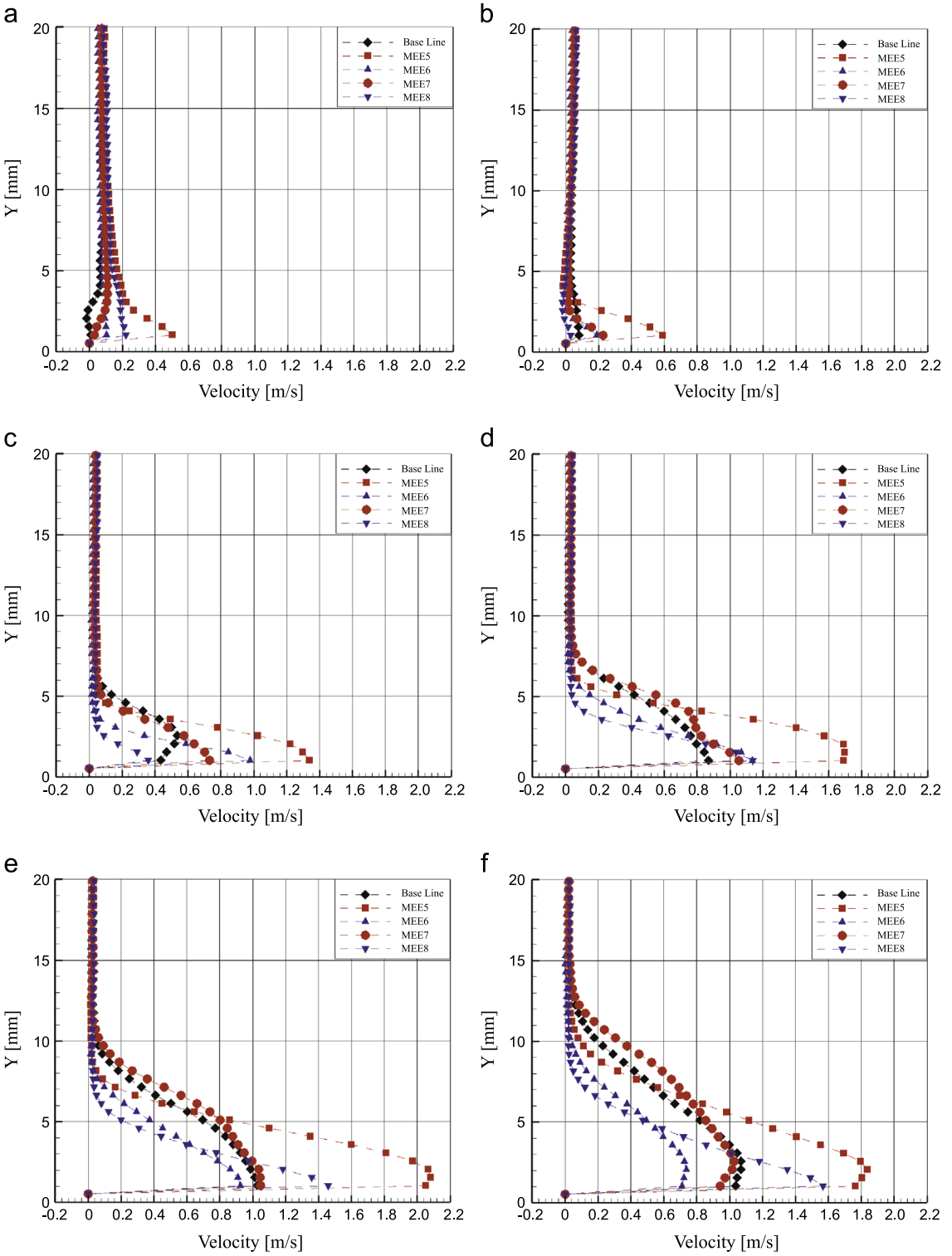

Fig. 7. Profiles of *x*-component of velocity downstream edge of exposed electrode: (a) $x=0$ mm (b) $x=10$ mm (c) $x=20$ mm (d) $x=30$ mm (e) $x=40$ mm and (f) $x=50$ mm.

with the shorter electrode located at the $x=0$ position, MEE5 and MEE6, produce the higher velocity jets. It is in this region where the electric field is modified due to the change of encapsulated electrode height.

At the $x=30$ mm position, Fig. 7(d), the MEE5 actuator induced jet accelerates to 1.7 m/s and the position of maximum velocity moves away from the wall. The other configurations continue to produce the maximum induced

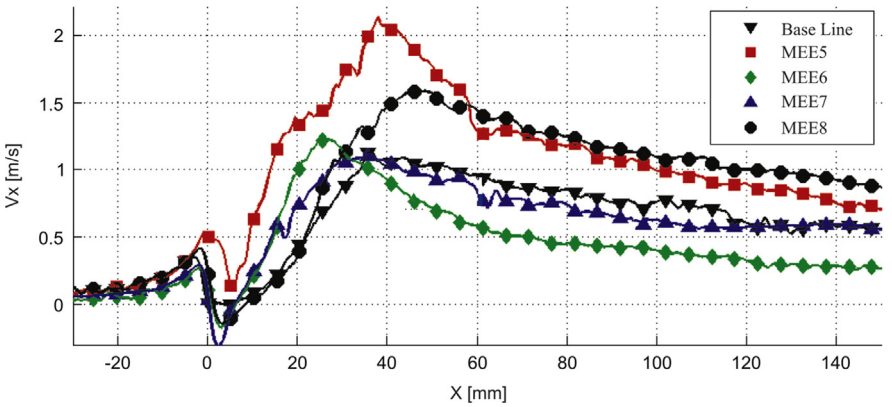

Fig. 8. Profiles of the x-component of velocity, along the x-axis, at $y=1$ mm.

velocity at the wall. The MEE6 configuration maximum velocity is only increased to 1.13 m/s, whereas the MEE7 configuration has accelerated to the same velocity from a lower velocity at $x=20$ mm. At this position all MEE cases produce a higher velocity than the baseline case although the jet produced by the baseline case is thicker than the MEE5, MEE6 and MEE8 configurations. The MEE6 case induces a velocity 11.2% higher than the baseline case.

At a downstream position of $x=40$ mm, Fig. 7(e), the MEE5 induced jet has accelerated to an excess of 2 m/s with the location of maximum velocity having moved away from the wall. The MEE8 induced jet has accelerated further, to over 1.4 m/s, while maintaining the maximum jet velocity at the wall. The MEE6 jet has retarded to 0.92 m/s with the maximum jet thickness moving away from the wall. It is at this position the encapsulated electrode height changes for the MEE7 and MEE8 actuators. The MEE7 maximum induced velocity is similar to the previous station although the profile is fuller and the jet is slightly thicker than the baseline case. The MEE8 jet becomes fuller with its jet thickness also increasing.

At the edge of the encapsulated electrode, $x=50$ mm Fig. 7(f), the MEE8 actuator velocity has accelerated to 1.56 m/s with the maximum velocity still closest to the wall. The MEE5 configuration still has the highest velocity although it has decreased in magnitude from the $x=40$ mm position and the position of maximum velocity moves further away from the wall due to momentum diffusion. The other actuator configurations all have jets of reduced velocity and increased thickness again due to momentum diffusion as the plasma is no longer accelerating the flow.

The velocity profiles for the x-component of velocity along the x-axis at a height of $y=1$ mm are shown in Fig. 8. It can be seen for all cases that V_x has a positive value upstream of the exposed electrode ($x=0$ in Fig. 8) and a negative value immediately downstream. This is due to the down flow region attracting air towards the 0 position. The MEE5 and MEE6 actuators both have steeper increases in V_x than the baseline case with the rate of increase being linear. The MEE7 and MEE8 actuators, with a longer initial electrode, have velocity profiles similar to the baseline case. While the rate of increase of velocity are similar the MEE8 actuator is able to increase velocity over the full extent of the encapsulated electrode. This results in the MEE8 configuration producing a higher induced velocity. For all of the actuator configurations the maximum induced velocity is achieved before the end of the encapsulated electrode. This suggests that the encapsulated electrode can be made shorter with the same velocity being recorded. At higher voltages, which mean higher electrical power, it is likely to see the peak at the downstream edge of encapsulated electrode for all of the MEE configurations which means the plasma will utilise the full extent of the encapsulated electrode. Downstream of the velocity peak the velocity reduces and the momentum is diffused.

Fig. 9 shows that there is a strong downward flow at the $x=0$ mm position while remaining close to zero at all other regions in the observation window. The downward flow in this region corresponds with the density measurements of Enloe et al. [23] where the downstream edge of the exposed electrode was seen to be pressurised. This establishes a pressure gradient that directs the pressure force in the downstream direction. The actuator with the greatest down flow magnitude also produces the highest induced velocity. The region immediately downstream of the exposed electrode is important in creating a higher induced velocity. The length over which the down flow peak is experienced is within 10 mm for all actuators with the exception of MEE5 and MEE8. These actuators produced the highest induced velocity and the highest magnitude down flow region. The down flow region is noticeable 30 mm downstream of the exposed electrode.

The effect of voltage on the induced velocity for the MEE actuators is presented in Fig. 10. The MEE5 actuator is able to induce a maximum velocity higher than all other actuator cases and 91.2% higher than the baseline case. Overall, the maximum induced velocity achieved was 2.48 m/s by the MEE7 configuration, 1 m/s higher than the baseline actuator at the same voltage. At 16 kV_{p-p} it produced a 40.3% higher induced velocity than the baseline case. Locating the first encapsulated electrode closer to the dielectric surface results in a higher velocity at lower voltages but the actuator is unable to operate at higher voltages due to the formation of filaments and degradation of the dielectric layer. Changing the distribution of the electrodes far away from the exposed electrode produces slight improvements at lower voltages and larger improvements at higher voltages and a larger voltage operating range.

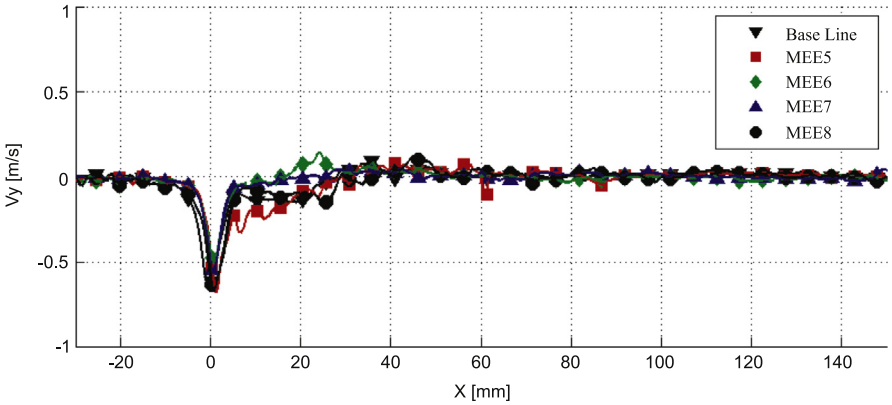

Fig. 9. Profiles of the y-component of velocity, along the x-axis, at $y=1$ mm.

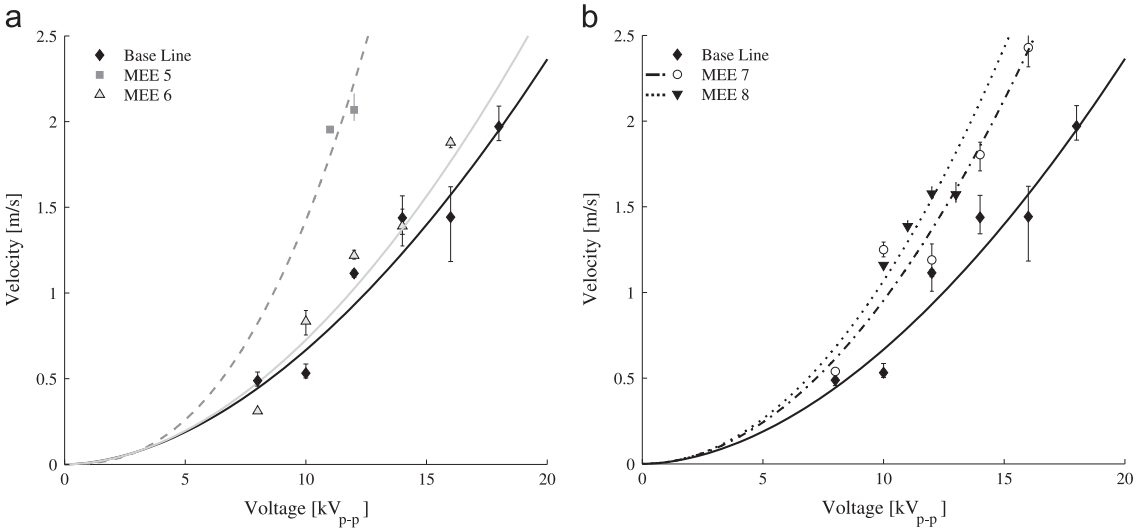

Fig. 10. Variation of maximum induced velocity with input voltage; (a) baseline, MEE5 and MEE6; and (b) baseline, MEE7 and MEE8.

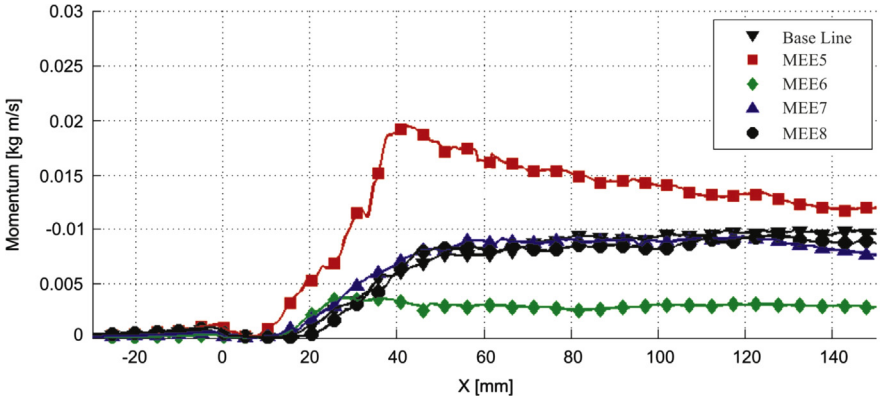

Fig. 11. Profiles of momentum along the x-axis, at $y=1$ mm.

The momentum profiles for the double MEE actuators are shown in Fig. 11. The MEE5 imparts momentum to the flow that is double the baseline actuator. At 12 kV_{p-p} the MEE5 actuator induces 71.4% more mechanical power than the baseline actuator. The momentum starts to increase at $x=10$ mm and continues to increase up to $x=40$ mm. The increase is linear and increases at a faster rate than the other double actuator cases. The MEE7 and MEE8 cases impart momentum with the same trend as the baseline case starting at $x=20$ mm and achieving a maximum of

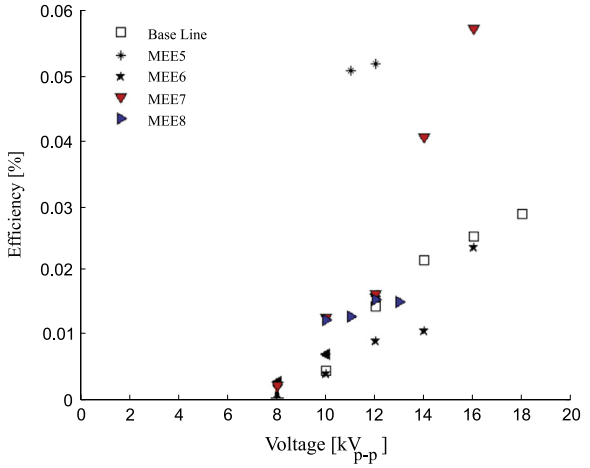

Fig. 12. Efficiencies of the actuator cases with varying voltage.

0.01 kg m/s. The MEE6 actuator, with a deep initial electrode, imparts flow at $x=20$ mm with the same rate of increases as the baseline case. The actuator cannot sustain the momentum addition for as long and achieves a maximum of 0.005 kg m/s.

3.4. Key performance characteristics

The efficiency of the actuators can be measured as a ratio of the mechanical power, given by Eq. (2), to the electrical power, where ρ is the air density, $v(Y)$ is the velocity profile and l is the electrode length. This is presented in Fig. 12.

$$\text{Power}_{mech} = \int_0^\infty \frac{1}{2}\rho v(Y)^3 \, l dY \tag{2}$$

This shows what percentage of the power supplied has been used to induce a jet in the flow. The efficiency of all of the actuator cases is very low with a maximum of 0.058% of electrical power being converted to mechanical power. This is in agreement with the magnitude of values obtained by Pons et al. [12]. The most efficient actuator is the MEE7 configuration with a long deep initial electrode followed by a short shallow electrode. This configuration was inefficient at the lower voltages and increased rapidly across the voltage range. The general trend for all of the cases is the higher the voltage the more efficient the actuator becomes. The actuators that are able to operate at higher voltages due to the positioning of a deeper initial electrode are able to convert more of the electrical energy into mechanical energy. The MEE5 case that induced the highest velocity jet operated the most efficiently at 12 kV_{p-p} but did not produce the highest efficiency because of the limitations on operating the actuator at higher voltages.

4. Conclusions

Manipulation of the encapsulated electrode has been shown to alter the performance of the dielectric barrier discharge plasma actuator. Locating the initial encapsulated electrode closer to the dielectric surface results in an earlier plasma ignition time and the plasma discharge being present for longer in the discharge cycle. This is the same result found when increasing the applied voltage to the baseline actuator.

Manipulation of the encapsulated electrode to locations closer to the dielectric surface results in induced velocities higher than the baseline case for a given voltage.

For the double MEE cases the maximum induced velocity was 91.2% higher than the baseline case for a 26.2% increase in power consumption. The MEE6 case required the least power using 14.32% less than the baseline case while still inducing a velocity 11.2% higher. Actuators with a deep initial electrode are able to induce higher velocities at lower power consumption than the standard actuator. At 16 kV_{p-p} the MEE7 actuator produced a 40.3% higher induced velocity than the baseline case while using 7.5% less power.

Actuators with a shallow initial electrode are able to impart more momentum and mechanical power into the flow. At 12 kV_{p-p} the MEE5 actuator induces 71.4% more mechanical power than the baseline actuator.

Actuators with shallow initial electrodes use more power than the baseline case at a given voltage. Conversely, actuators with a deep initial electrode use less power than the baseline case at a given voltage.

Actuator MEE7 with a deep initial electrode achieved the highest induced velocity of 2.48 m/s. This is because the actuator can operate at higher voltages without dielectric layer breakdown.

The efficiency of the plasma actuator at imparting mechanical power into the flow is low, 0.05% maximum in the cases tested.

Actuators with plasma lasting for longer portions of the cycle do not always produce higher velocity induced jets. This highlights the importance of the quench period.

Acknowledgements

The authors are indebted to the technical and administrative staff at The University of Manchester for their assistance. The authors would also like to thank Dr. Tohid Erfani for his technical advice. This work was supported by Engineering and Physical Sciences Research Council (EPSRC Grant Reference: EP/H500154/1).

References

[1] T.C. Corke, C.L. Enloe, S.P. Wilkinson, Dielectric barrier discharge plasma actuators for flow control, Annu. Rev. Fluid Mech. 42 (2010) 505–529.
[2] E. Moreau, Airflow control by non-thermal plasma actuators, J. Phys. D: Appl. Phys. 40 (2007) 605–636.
[3] R. Erfani, H. Zare-Behtash, K. Kontis, Influence of shock wave propagation on dielectric barrier discharge plasma actuator performance, J. Phys. D: Appl. Phys. 45 (22) (2012) 225201.
[4] J.R. Roth, D.M. Sherman, S.P. Wilkinson, Electrohydrodynamic flow control with a glow-discharge surface plasma, AIAA J. 38 (7) (2000) 1166–1172.
[5] M. Forte, J. Jolibois, F. Baudoin, E. Moreau, G. Touchard, M. Cazalens, Optimization of a dielectric barrier discharge actuator and non-stationary measurements of the induced flow velocity-application to airflow control, in: 3rd AIAA Flow Control Conference, Paper Number AIAA, 2006, pp. 2006–2863.

[6] R. Erfani, T. Erfani, S.V. Utyuzhnikov, K. Kontis, Optimisation of multiple encapsulated electrode plasma actuator, Aerosp. Sci. Technol. 26 (1) (2013) 120–127.
[7] C.L. Enloe, T.E. McLaughlin, R.D. VanDyken, K.D. Kachner, E.J. Jumper, T.C. Corke, M. Post, O. Haddad, Mechanisms and responses of a single dielectric barrier plasma actuator: geometric effects, AIAA J. 42 (3) (2004) 595–604.
[8] C.L. Enloe, T.E. McLaughlin, R.D. VanDyken, K.D. Kachner, E.J. Jumper, T.C. Corke, Mechanisms and responses of a single dielectric barrier plasma actuator: plasma morphology, AIAA J. 42 (3) (2004) 589–594.
[9] R. Hippler, H. Kersten, M. Schmidt, K.H. Schoenbach, Low Temperature Plasmas: Fundamentals, Technologies and Techniques, vol. 1, Wiley-VCH, 2008.
[10] R. Erfani, H. Zare-Behtash, K. Kontis, Plasma actuator: influence of dielectric surface temperature, Exp. Therm. Fluid Sci. 42 (2012) 258–264.
[11] M. Forte, J. Jolibois, J. Pons, E. Moreau, G. Touchard, M. Cazalens, Optimization of a dielectric barrier discharge actuator by stationary and non-stationary measurements of the induced flow velocity: application to airflow control, Exp. Fluids 43 (6) (2007) 917–928.
[12] J. Pons, E. Moreau, G. Touchard, Asymmetric surface dielectric barrier discharge in air at atmospheric pressure: electrical properties and induced airflow characteristics, J. Phys. D: Appl. Phys. 38 (2005) 3635.
[13] J.R. Roth, X. Dai, Optimization of the aerodynamic plasma actuator as an electrohydrodynamic (EHD) electrical device, in: 44th AIAA Aerospace Sciences Meeting and Exhibit, Reno, Paper Number AIAA-2006-1203, 2006.
[14] M.L. Post, T.C. Corke, Separation control on high angle of attack airfoil using plasma actuators, AIAA J. 42 (11) (2004) 2177–2184.
[15] J. Huang, T.C. Corke, F.O. Thomas, Plasma actuators for separation control of low-pressure turbine blades, AIAA J. 44 (1) (2006) 51–57.
[16] C. He, T.C. Corke, M.P. Patel, Plasma flaps and slats: an application of weakly ionized plasma actuators, J. Aircr. 46 (3) (2009) 864–873.
[17] C. Hale, R. Erfani, K. Kontis, Increasing the induced velocity of dielectric barrier discharge plasma actuators, in: CEAS 2009 European Air and Space Conference, 2009.
[18] C. Hale, R. Erfani, K. Kontis, Plasma actuators with multiple encapsulated electrodes to influence the induced velocity, in: 48th AIAA Aerospace Sciences Meeting Including the New Horizons Forum and Aerospace Exposition, Paper Number AIAA-2010-1223, 2010.
[19] C. Hale, R. Erfani, K. Kontis, Plasma actuators with multiple encapsulated electrodes to influence the induced velocity: further configurations, in: 40th Fluid Dynamics Conference and Exhibit, Paper Number AIAA-2010-5106, 2010.
[20] T. Ukai, H. Zare-Behtash, E. Erdem, K.H. Lo, K. Kontis, S. Obayashi, Effectiveness of jet location on mixing characteristics inside a cavity in supersonic flow, Exp. Therm. Fluid Sci. 52 (2014) 59–67.
[21] M.L. Post, T.C. Corke, Separation control using plasmas actuators—stationary and oscillating airfoils, in: 42nd AIAA Aerospace Sciences Meeting and Exhibit, 2004.
[22] A. Santhanakrishnan, J.D. Jacob, Flow control with plasma synthetic jet actuators, J. Phys.-Lond.-D: Appl. Phys. 40 (3) (2007) 637.
[23] C.L. Enloe, T.E. McLaughlin, G.I. Font, J.W. Baughn, Parameterization of temporal structure in the single-dielectric-barrier aerodynamic plasma actuator, AIAA J. 44 (6) (2006) 1127–1136.